

Neutrino mass spectroscopy using Er^{3+} ions placed at inversion center of host crystals

H. Hara, N. Sasao, A. Yoshimi, and M. Yoshimura
Research Institute for Interdisciplinary Science, Okayama University
Tsushima-naka 3-1-1 Kita-ku Okayama 700-8530 Japan

arXiv:1910.14318v1 [hep-ph] 31 Oct 2019

ABSTRACT

We propose neutrino mass spectroscopy using $\text{Er}^{3+}:\text{Cs}_2\text{NaYF}_6$ or $:\text{Y}_2\text{O}_3$ crystal placed in hollow of a Bragg fiber as a target system. Unknown neutrino parameters and properties such as the lightest neutrino mass, Majorana/Dirac distinction, and CP violating phases can be explored by measuring scattered photons (γ) along the excitation (and fiber) axis by varying Raman trigger (γ_0) directions, in Er^{3+} de-excitation process from $|e\rangle$ state to $|g\rangle$ state; $|e\rangle, |e\rangle + \gamma_0 \rightarrow |g\rangle + \gamma + \nu_i \bar{\nu}_j, \nu_i, i = 1, 2, 3$ being a mass-resolved neutrino state. Rates and required level of QED background rejection are calculated using measured data of the target system.

Keywords Neutrino mass, Majorana fermion, lanthanoid ions at inversion center, Er^{3+} , Bragg fiber

1 Introduction

In two preceding papers [1], [2] some of us explored the possibility of using lanthanoid ions doped in crystals in order to open a pathway towards resolving remaining important issues of neutrino properties: (1) the smallest neutrino mass in the three flavor neutrino scheme, (2) Majorana/Dirac distinction along with their CP violating phases. The purpose of the present work is to investigate schemes using promising target ion Er^{3+} for the same objectives. Er^{3+} ions placed at inversion center of host crystals such as Cs_2NaYF_6 and Y_2O_3 are attractive candidates of neutrino mass spectroscopy [3], since 100 % Er replacing Y site is possible, hence a high density target may be realized. Moreover, this ion is considerably different from Sm^{2+} previously studied [2] in the energy level structure, and above all it is a Kramers ion for which a magnetic control may work in interesting manners.

Experimental progress towards neutrino mass spectroscopy [3] relies on the principle of macro-coherence which makes otherwise tiny rates large enough of experimental interest. Its verification in weak QED processes has been demonstrated in [4], realizing $\sim 10^{18}$ effective enhancement over spontaneous emission rate. The next important step is to fabricate solid targets, and for this purpose lanthanoid ions are ideal due to its narrow optical width of state levels. Reduction of macro-coherently amplified QED backgrounds is the main issue of discussion, since rates can be made large enough for detection. The largest QED background is rejected by a kinetic constraint and the next largest by a symmetry of host crystals, presence of inversion center [2]. We employ Bragg fiber [5], [6] to reject still remaining backgrounds.

We use the natural unit of $\hbar = c = 1$ throughout the present work unless otherwise stated. Useful numbers to remember are $1 \text{ eV} = 1.5 \times 10^{15} \text{ sec}^{-1}$ and its inverse = 1,240 nm of laser wavelength, Avogadro number $\text{cm}^{-3} = 7.6 \times 10^{-15} \text{ eV}^3$, $G_F^2 \text{ eV}^5 = 2.1 \times 10^{-31} \text{ sec}^{-1}$. Atomic physics often uses a unit of energy, cm^{-1} , and it is related to eV by $10^4 \text{ cm}^{-1} = 1.24 \text{ eV}$.

2 Three RANP schemes and rejection of major QED background

Macro-coherent, double resonant Raman-stimulated neutrino pair emission (RANP) [1] has three possible schemes which differ in where neutrino pair is emitted, as depicted in Fig(1). In all three schemes the neutrino pair $\nu_i \bar{\nu}_j$ (or simply (ij)) emission has a vertex given by

$$\langle b | \vec{S} \cdot \vec{N}_{ij} e^{i(\vec{p}_1 + \vec{p}_2) \cdot \vec{x}} | a \rangle, \quad (1)$$

where \vec{S} is the total $4f^n$ electron spin operator of lanthanoid ions, and $\vec{p}_i, i = 1, 2$'s are momenta of emitted neutrinos. Neutrino pair current amplitude \vec{N}_{ij} is readily calculable [3] in the standard electroweak theory assuming finite neutrino masses of either Dirac or Majorana type. Rate calculation proceeds, first taking square of the amplitude (1) and summing over non-detectable neutrino helicities and momenta. This neutrino variable integration can be done independently of atomic part calculation. We assume the long wavelength approximation in the plane wave factor, the pair momentum being of order eV range or less, hence $|\vec{p}_1 + \vec{p}_2| \ll$ inverse of atomic size typically of order keV. With $e^{i(\vec{p}_1 + \vec{p}_2) \cdot \vec{x}} = 1$, one is led to the neutrino factor (later

given by eq.(5)) times atomic matrix element $|\langle b|\vec{S}|a\rangle|^2$ for unpolarized ion targets we assume hereafter. Electromagnetic vertex responsible for photon emission and absorption is thus dominantly of magnetic dipole (M1) type, and satisfies the selection rule of atomic quantum number change, $|\Delta J| \leq 1$.

For atomic de-excitation path $|e\rangle \rightarrow |p\rangle \rightarrow |q\rangle \rightarrow |g\rangle$ of Fig(1) we assume $|\Delta J_{ab}| \leq 1$ for all atomic transitions, $|a\rangle \rightarrow |b\rangle$, in order to maximize RANP rates. In many lanthanoid ions energies of lower J -manifolds increase according to either decreasing or increasing J values, as exemplified in Fig(3) for Er^{3+} . We thus use three lowest J -manifolds to satisfy the selection rule $|\Delta J_{ab}| \leq 1$ at each transition. In [2] we studied Sm^{2+} ion at inversion center of host crystals, which requires challenging infrared lasers. In the present work we examine trivalent lanthanoid ion Er^{3+} of different level spacing doped at inversion center of Y in Cs_2NaYF_6 and Y_2O_3 , [7], [8], [9], which has O_h crystal point group symmetry. 100% doping (or replacement) gives Er^{3+} number densities, $5.40 \times 10^{21} \text{cm}^{-3}$ for Cs_2NaYF_6 and $2.72 \times 10^{22} \text{cm}^{-3}$ for Y_2O_3 .

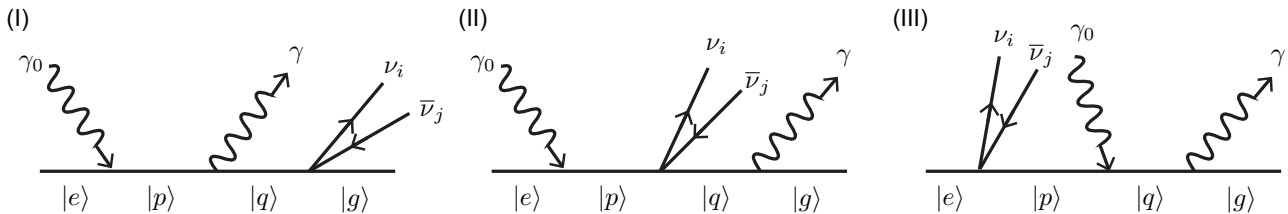


Figure 1: Three schemes of Raman-stimulated neutrino pair emission in de-excitation path, $|e\rangle \rightarrow |p\rangle \rightarrow |q\rangle \rightarrow |g\rangle$.

As discussed in [1] and [2], the squared mass function \mathcal{M}^2 plays crucial roles both in the criterion of dominant QED background rejection, namely McQ3 of [10], and in RANP angular spectrum. The function at resonances of Raman trigger γ_0 of energy ω_0 and scattered γ of energy ω is defined by $\mathcal{M}^2 = (p_{eg} + k_0 - k)^2$, $p_{eg} = (\epsilon_{eg}, r\epsilon_{eg}, 0, 0)$ ($\vec{p}_{eg} = r\epsilon_{eg}\vec{e}_x$ with \vec{e}_x the unit vector along the excitation axis is the spatial phase vector imprinted at excitation). The squared mass function is thus a function of two angles $\mathcal{M}^2(\theta_0, \theta)$, the Raman trigger direction θ_0 and scattered direction θ both measured from the excitation direction. The phase magnitude parameter r depends on excitation scheme one adopts, and is unity, $r = 1$, for a single laser or two-laser excitation along the same direction. From the reason stated below we fix the scattered direction along the excitation axis, hence $\theta = 0$ or π . Under this circumstance,

$$\mathcal{M}^2(\theta_0, 0) = 4\omega_0(r\epsilon_{eg} - \omega) \sin^2 \frac{\theta_0}{2} + 2(1 - r)\epsilon_{eg} \left(\omega_0 - \omega + \frac{1 + r}{2}\epsilon_{eg} \right). \quad (2)$$

RANP experiments should be conducted at trigger directions when the quantity $\mathcal{M}^2(\theta_0, 0)$ is positive, with its values close to neutrino pair masses $(m_i + m_j)^2$. As in [1] and [2], we take the double resonance scheme to fix ω_0 and ω for maximal RANP rates. Scheme I gives $\omega_0 = \epsilon_{pe}$ and $\omega = \epsilon_{pq}$, while Scheme II $\omega_0 = \epsilon_{pe}$ and $\omega = \epsilon_{qg}$.

It is difficult to satisfy the macro-coherence condition, namely the momentum and the energy conservation given by 4-momentum notation, $p_{eg} + k_0 = k + p_1 + p_2$ with p_i two neutrino energy-momentum, near

the excitation axis for $r = 1$. As seen from eq.(2), $\mathcal{M}^2(\theta_0, 0)$ tends to be negative for $r > 1$, hence we take $0 < r < 1$ except in the case of $\theta = \pi$ later. For counter-propagating two-laser irradiation for excitation two excitation photons have energies of $(1 \pm r)\epsilon_{eg}/2$. In all paths discussed below we first verify the positivity of squared mass function $\mathcal{M}^2(\theta_0, 0) > 0$ to ensure absence of McQ3 background.

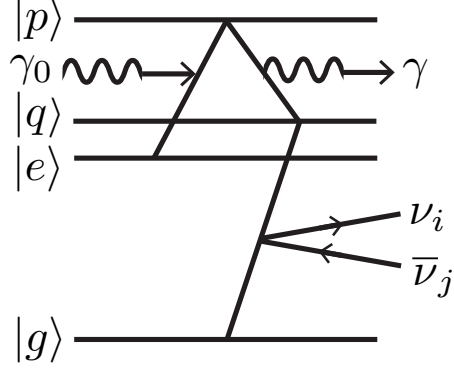


Figure 2: Energy level diagrams indicating absorption and emission of photons and a neutrino-pair corresponding to scheme I.

3 Raman stimulated neutrino pair emission rate

In the third order of perturbation theory which regards four-Fermi interaction as a primary hamiltonian, the squared amplitude in scheme I is given by

$$|\mathcal{A}|^2 = \frac{|H_{pe}^\gamma H_{pq}^\gamma H_{qg}^W|^2}{((\omega_0 - \epsilon_{pe})^2 + \gamma_1^2/4) ((E_1 + E_2 - \epsilon_{qg})^2 + \gamma_2^2/4)} 2\pi\delta(\epsilon_{eg} + \omega_0 - E_1 - E_2 - \omega), \quad (3)$$

ignoring irrelevant terms. A double resonance occurs at $\omega_0 = \epsilon_{pe}$ and $E_1 + E_2 = \epsilon_{qg}$ (equivalent to $\omega = \epsilon_{pq}$). Dominant electromagnetic vertex H_{ab}^γ among $4f^{11}$ J -manifolds is of magnetic dipole type with a small admixture of electric dipole induced by crystal field effects as first pointed out in [11].

Differential rate for unpolarized targets is calculated, by using the formula of [2], as

$$\frac{d\Gamma_{\text{RANP}}}{d\Omega} = 288\pi \frac{\gamma_{pe}\gamma_{pq}G_F^2}{\epsilon_{pe}^2\epsilon_{pq}^2} \frac{n^4V}{\Delta\omega_0(\gamma_e^2 + \gamma_q^2)^{3/2}} \eta \sum_{ij} F_{ij}(\theta_0) \Theta(\mathcal{M}^2(\theta_0, 0) - (m_i + m_j)^2), \quad (4)$$

$$F_{ij}(\theta_0) = \frac{1}{8\pi} \left\{ \left(1 - \frac{(m_i + m_j)^2}{\mathcal{M}^2(\theta_0, 0)} \right) \left(1 - \frac{(m_i - m_j)^2}{\mathcal{M}^2(\theta_0, 0)} \right) \right\}^{1/2} \left[\frac{1}{2} |b_{ij}|^2 (\mathcal{M}^2(\theta_0, 0) - m_i^2 - m_j^2) - \delta_M \Re(b_{ij}^2) m_i m_j \right], \quad (5)$$

$$b_{ij} = U_{ei}^* U_{ej} - \frac{1}{2} \delta_{ij}, \quad (6)$$

where n is the number density of excited target ions. The angular acceptance factor $d\Omega$ shall be estimated later when we discuss an experimental layout. From the macro-coherence condition of energy-momentum

conservation the squared mass function is equal to the invariant squared mass of the neutrino-pair system: $\mathcal{M}^2(\theta_0, \theta) = (p_1 + p_2)^2$. The 3×3 unitary matrix $(U_{ei}), i = 1, 2, 3$, refers to the neutrino mass mixing [13].

The parameter η is defined by laser power divided by $|\rho_{eg}|^2 \epsilon_{pe} n / 2$ where $\rho_{eg} = |c_e^* c_g|^2$ with c_a the probability amplitude of state $|a\rangle$ in a purely quantum mechanical system without dissipation. In actual system η is time varying $\eta(t)$, and may be calculated using the Maxwell-Bloch equation, a coupled system of non-linear and partial differential equations for fields and density matrix elements. Systematic calculation of $\eta(t)$ is beyond the scope of the present work, but its sample calculations are given in [3]. We introduce a time independent η in the present work.

Dependence on $\propto n^4 V$ of RANP rate (4) is understood as follows. Rate of Raman stimulated resonant weak process is given by a product of Raman rate times weak process rate multiplied by the lasting lifetime of intermediates state, hence $d\Gamma_{RW} = 4d\Gamma_R d\Gamma_W / \sqrt{\gamma_e^2 + \gamma_q^2}$ [2]. Macro-coherence gives $n^2 V (2\pi)^3 \delta(\vec{p}_{eg} + \vec{k}_0 - \vec{k} - \vec{p}_1 - \vec{p}_2)$ with the momentum conservation for the entire process. With the resonance dictated by trigger laser at frequency $\omega_0 = \epsilon_{pe}$, the momentum conservation is maintained in Raman and weak processes simultaneously, $\vec{p}_{eg} + \vec{k}_0 = \vec{k}$ and $\vec{p}_1 + \vec{p}_2 = 0$, which gives an extra n dependence as shown in [1], [2]. Another n factor arises from incident trigger laser power E_0^2 related to definition or the η factor.

According to [8], calculated radiative decay rates of 10% doped Er^{3+} in host Cs_2NaYF_6 are

$${}^4\text{I}_{13/2} \rightarrow {}^4\text{I}_{15/2} : (24.82^{\text{MD}} + 2.46^{\text{ED}}) \text{sec}^{-1}, \quad (7)$$

$${}^4\text{I}_{11/2} \rightarrow {}^4\text{I}_{13/2} : (4.26^{\text{MD}} + 0.42^{\text{ED}}) \text{sec}^{-1}, \quad {}^4\text{I}_{11/2} \rightarrow {}^4\text{I}_{15/2} : 4.13^{\text{ED}} \text{sec}^{-1}. \quad (8)$$

MD(M1) and ED(E1) refer to magnetic and electric dipole transition rates calculated according to modified Judd-Ofelt theory [12]. Squared atomic vertex (magnetic or electric dipole) amplitudes are equal to $3\pi\gamma_{ab}/\epsilon_{ab}^3$, which was used in RANP rate formula, eq(4). We further assume that radiative transition rates between two specific Stark states in two different J -manifolds are not much different for different Stark states. Stark level splitting caused by crystal field has been calculated and compared with experimental data in [7]. In the adopted de-excitation path we used experimental results obtained in this work. For state $|q\rangle$ of ${}^4\text{I}'_{13/2}$ manifold there are other choices of Stark levels: 6586, 6552, 6510 cm^{-1} 's, the last one being the case of Raman elastic scattering.

Non-radiative decay rates are expected to be large for higher energy states. According to [8] decay rate of ${}^4\text{I}_{13/2}$ of lower energy is mainly radiative, but the next lower ${}^4\text{I}_{11/2}$ is dominated by non-radiative rates (non-radiative is ten times larger than radiative) at room temperature. We need to experimentally investigate non-radiative decay rates ${}^4\text{I}_{11/2}$ at lower temperatures to examine how much radiative rates increase compared with non-radiative rates, but in the present work we shall assume dominance of radiative ${}^4\text{I}_{11/2}$ decay for simplicity.

We first consider the following de-excitation path of scheme I for $\text{Er}^{3+} : \text{Cs}_2\text{NaYF}_6$,

Path A: $\text{Er}^{3+}, {}^4\text{I}_{13/2} \rightarrow {}^4\text{I}_{11/2} \rightarrow {}^4\text{I}'_{13/2} \rightarrow {}^4\text{I}_{15/2}$

${}^4\text{I}_{13/2}, 6510 \text{ cm}^{-1}$ (805.8 meV), ${}^4\text{I}_{11/2}, 10227 \text{ cm}^{-1}$ (1266 meV), ${}^4\text{I}'_{13/2}, 6883 \text{ cm}^{-1}$ (852 meV).

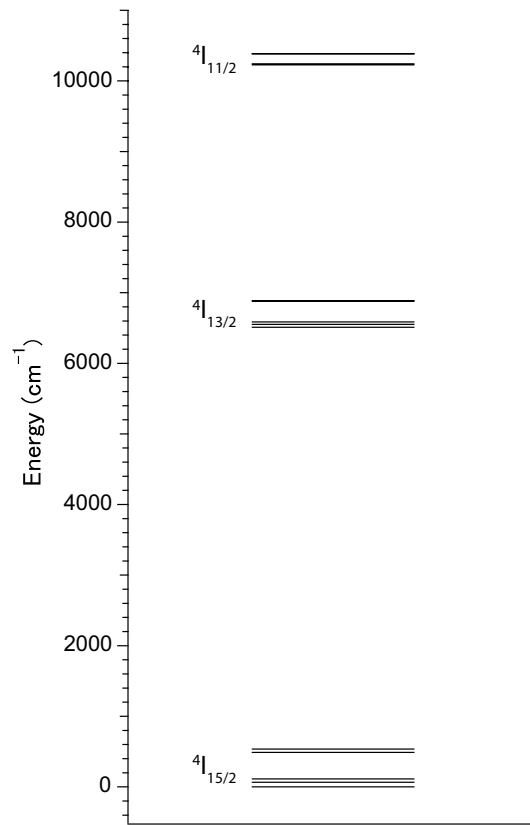


Figure 3: Three lower J - manifold energy level diagram of $\text{Er}^{3+}:\text{Cs}_2\text{NaYF}_6$.

Angular distributions: Er3+

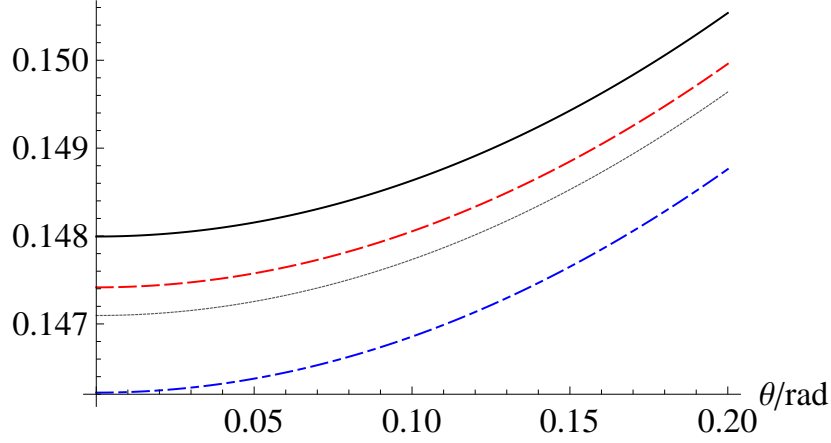


Figure 4: Raman trigger angular distribution given by $8\pi \sum_{ij} F_{ij}(\theta)$ in eV^2 unit, assuming $r = 0.8$ in scheme A: Smallest neutrino mass of $m_1 = 5, 20\text{meV}$'s of Dirac NH in solid and dotted blacks, and Majorana NH in dashed red and dash-dotted blue. CP violating phases are assumed to vanish. Absolute rate is derived by multiplying $R\Delta\Omega$, $R = 5.2 \times 10^7 \text{sec}^{-1} \left(\frac{n}{10^{15}\text{cm}^{-3}}\right)^4 \frac{V}{10^{-2}\text{cm}^3} \frac{100\text{MHz}}{\Delta\nu_0} \eta$, with R defined in eq.(9) and $\Delta\Omega$ the angular acceptance factor.

Relevant dipole moment values in the formula (4) are

$$\frac{\gamma_{pe}}{\epsilon_{pe}^2} = \frac{4.68\text{sec}^{-1}}{0.460^2\text{eV}^2} \sim 5.74 \times 10^{-13}\text{eV}^{-1}, \quad \frac{\gamma_{pq}}{\epsilon_{pq}^2} \sim 1.79 \times 10^{-14}\text{eV}^{-1},$$

$$(\gamma_e^2 + \gamma_q^2)^{3/2} \sim 1.6 \times 10^{-41} \text{eV}^3,$$

in eV unit, using data of [7] and [8]. Taking $\Delta\omega_0 = 2\pi\Delta\nu_0 = 2\pi 100\text{MHz}$ for the trigger laser width gives

$$\frac{d\Gamma_{\text{RANP}}}{d\Omega} = R \frac{8\pi \sum_{ij} F_{ij}(\theta)}{\text{eV}^2}, \quad R = 5.2 \times 10^7 \text{sec}^{-1} \left(\frac{n}{10^{15}\text{cm}^{-3}}\right)^4 \frac{V}{10^{-2}\text{cm}^3} \frac{100\text{MHz}}{\Delta\nu_0} \eta. \quad (9)$$

For convenience we changed the notation θ_0 to θ . In the figures of angular distributions this eV unit is used, giving $8\pi \sum_{ij} F_{ij}(\theta)$ of order $0.1 \sim 0.01 \text{eV}^2$. Hence differential RANP rates of path A are of order 10^6sec^{-1} assuming the same $n, V, \Delta\nu_0$ values.

In Fig(4) we show the sensitivity to the smallest neutrino mass and to Majorana/Dirac distinction. In all calculations of rates we assume CP violating phases to vanish (case of CP conservation) for simplicity. The largest threshold rises are at the paired neutrino mass of (12) and (33) where we order neutrino masses as $m_1 < m_2 < m_3$. Input neutrino mass for numerical rate calculations is the smallest neutrino mass m_1 and we determine other masses using data of [13] along with mixing angles.

4 Bragg fiber to reject remaining QED backgrounds

Macro-coherently amplified QED backgrounds have been classified in [10] and they are called McQn, when n number of photons are involved. Due to the host crystal symmetry of inversion center, McQ4 rejection containing E1 transitions is nearly complete, but McQ4 events caused by four vertexes of M1 operators are still large. We shall use a Bragg fiber to suppress extra two-photon emission replacing neutrino-pair [5], [6]. The idea is that due to an effective transverse photon mass in a kind of photonic crystal or wave guide some of two-photon emission may be prohibited in the Bragg fiber, but neutrino pair emission is not. To determine how much suppression we gain by this device it is necessary to estimate McQ4 event rate of Er^{3+} doped crystals.

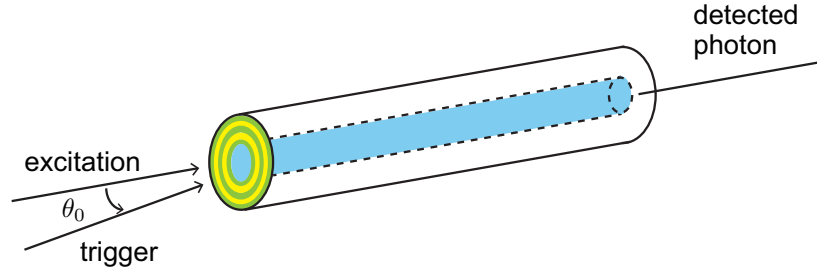


Figure 5: Illustration of an experimental layout. Target crystal in light blue color is placed inside a hollow of Bragg fiber consisting of paired dielectric layers with a refractive index contrast. Emitted and triggered photons can propagate only along the Bragg fiber.

In [2] the ratio of McQ4 to RANP differential rates in scheme I was calculated, to give

$$\frac{\Gamma_{\text{McQ4}}(\theta)}{\Gamma_{\text{RANP}}(\theta)} = \frac{\Gamma_{2\gamma}(\theta)}{\Gamma_{2\nu}(\theta)}, \quad (10)$$

$$\Gamma_{2\gamma}(\theta) = \frac{9\pi}{8} \frac{n}{\sqrt{\epsilon_{qg}^2 - \mathcal{M}^2(\theta)}} \sum_x \frac{\gamma_{xq}\gamma_{xg}}{\epsilon_{xq}^2 \epsilon_{xg}^2} \int_{\omega_-}^{\omega_+} d\omega \omega (\epsilon_{qg} - \omega) \left(\frac{1}{\epsilon_{xq} + \omega} + \frac{1}{\epsilon_{xg} - \omega} \right)^2, \quad (11)$$

$$\Gamma_{2\nu}(\theta) = \frac{G_F^2 n}{2} \sum_{ij} F_{ij}(\theta) \Theta(\mathcal{M}^2(\theta) - (m_i + m_j)^2), \quad (12)$$

with $\omega_{\pm} = \frac{1}{2}(\epsilon_{qg} \pm \sqrt{\epsilon_{qg}^2 - \mathcal{M}^2(\theta)})$. We may approximate the summation over upper levels, x , in eq.(11) by taking the lowest upper level, $x = p$. The resulting single integral is calculated numerically, which turns out a slowly decreasing function of θ , and $\sim 1.6\text{eV}$ in the region of $\theta \leq 0.1$ in path A. Using this value we obtain the ratio,

$$\frac{\Gamma_{\text{McQ4}}(\theta)}{\Gamma_{\text{RANP}}(\theta)} \sim \frac{18\pi^2}{G_F^2} \frac{\gamma_{pq}\gamma_{pg}}{\epsilon_{pq}^2 \epsilon_{pg}^2} \frac{1.6\text{eV}}{\epsilon_{qg}} \frac{\text{eV}^2}{8\pi \sum_{ij} F_{ij}(\theta) \Theta(\mathcal{M}^2(\theta) - (m_i + m_j)^2)}, \quad (13)$$

with an approximation $\mathcal{M}^2(\theta) \ll \epsilon_{qg}^2$. Numerically, the ratio is of order 5×10^{21} times the inverse of angular rate of order 10, giving of order 10^{22} ratio for Er^{3+} .

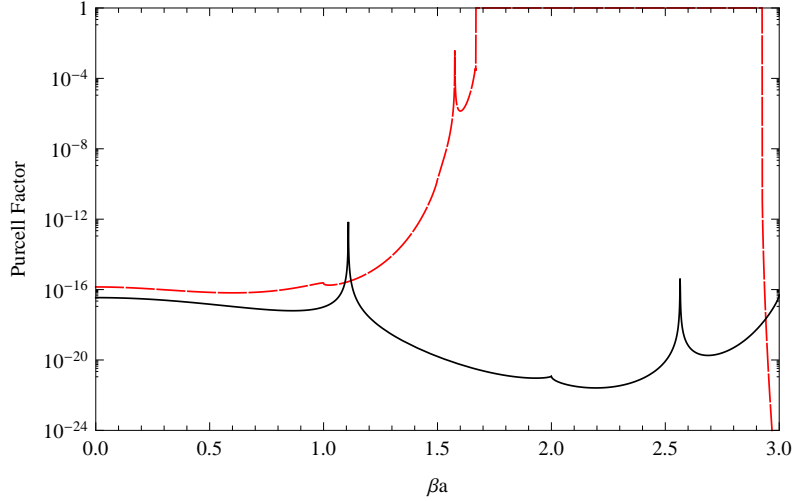


Figure 6: Purcell factor (ratio of intensities inside of Bragg fiber to that in free space) vs β , the component of photon wavevectors along the fiber axis; $\omega a = 1$ in long-dashed red and $\omega a = 2$ in solid black where ω and $a(= a_1 + a_2)$ are, respectively, the frequency of the photon and the thickness of one paired layer. In the case of the two (single) photon emission between $|p\rangle$ and $|q\rangle$ states, each photon is suppressed by a factor shown in the red $\omega a = 1$ (the black $\omega a = 2$) line. Other parameters used in the calculation are: $a = 2a_1 = 2a_2 \simeq 11 \mu\text{m}$, $n_1 = 2$, $n_2 = 5$ and the number of layers $N_p = 35$. Note that the maximum βa in the case of the two (single) photon emission is $n_0 = 1.5$ ($n_0 \times 2 = 3$) where n_0 , the refractive index of target crystal, is assumed to be 1.5.

Since it is easier to forbid emission of lower energy photons in Bragg fibers of realistic layer thickness, we calculate RANP angular distributions arising from de-excitation paths in scheme II that use smaller Stark level splitting within the same J -manifold. As an example we use is

Path B: $\text{Er}^{3+}:\text{Cs}_2\text{NaYF}_6$ scheme II; ${}^4\text{I}_{15/2}$ 537 $\text{cm}^{-1} \rightarrow {}^4\text{I}_{13/2}$ 6883 $\text{cm}^{-1} \rightarrow {}^4\text{I}'_{13/2}$ 6586, 6552, 6510 $\text{cm}^{-1} \rightarrow {}^4\text{I}_{15/2}$ 0 cm^{-1} .

Explorable neutrino pair mass is limited by intra- J manifold spacing ϵ_{pq} . It is necessary to have trigger photons near the backward direction, $\theta_0 \approx \pi$ to the excitation axis. With small $\epsilon_{eg} \sim 66.5$ meV, Raman type of excitation with a large r is required. The value r is chosen such that the center of mass system of the neutrino pair is at rest in the laboratory ($\vec{p}_1 + \vec{p}_2 = 0$). In this case, two photons by the McQ4 process have equal energy and thus background suppression by Bragg fiber becomes easier and efficient. This way we derive $r = 24.08$, and we calculate rates with this value. The angular acceptance factor $\Delta\Omega$ is estimated by placing a photon detector at the end of cylindrical fiber, to give $\Delta\Omega \sim \pi d/l$ with d the cylinder radius and l its length.

The necessary number of paired dielectrics of refractive index contrast (2, 5) is now worked out to search for the forbidden region of McQ4 events. An example of suppression factors inside a Bragg fiber given by the Purcell factor [14] is illustrated in Fig(6). This calculation uses an approximation that replaces the cylindrical layer configuration of Bragg fiber by the slab configuration much easier for estimation. This example may be used for two-photons emitted nearly back to back in any direction with equal energy $\omega_*, 2\omega_* = \epsilon_{pq}$, mimicking two-photon emission of total momentum zero. The suppression factor of two-photon emission with $\omega_*a = 1$ (red curve in Fig(6)) is less than 10^{-24} , sufficient to kill McQ4 events.

A different type of McQ4 event in which extra photons $\gamma_1\gamma_2$ are emitted between $|q\rangle$ and $|g\rangle$ of level spacing ~ 800 meV is inevitable in the kind of Bragg fiber discussed here. With a signal photon of energy $37 \sim 46$ meV suppressed by $< 10^{-16}$ in the Bragg fiber, McQ4 rate is estimated 10^6 relative to RANP rate. Due to different event topology this McQ4 events are distinguishable from RANP signals, but depletion in the state $|p\rangle$ gives effective reduction of RANP rate by 10^6 . It is necessary to make simulations to compute depletion factor more precisely. In Fig(7) we illustrate a result of angular distribution for this path.

5 Prospects

An explorable range of neutrino mass is limited by realistic fabrication of Bragg fiber whose layer sizes are several tens of micron, inverse of 25 meV, at minimum. Since one of the strongest thresholds is (12) pair, this limits the pair mass less than $\sqrt{m_1^2 + 10^2} + m_1 = 25$ meV, which corresponds to the smallest neutrino mass $m_1 < 11$ meV. (3, 3) threshold identification requires rejection of McQ4 extra photon of energy ~ 60 meV, which is difficult to realize in the present scheme of Bragg fiber.

An equally interesting crystal is Y_2O_3 which can host Er^{3+} at 100%. All seven Kramers doublets of $\text{Er}^{3+} {}^4\text{I}_{13/2}$ in this crystal are identified with measured Stark level energies: 6510, 6542, 6588, 6594, 6684, 6840, 6867 cm^{-1} [9]. With a high resolution of detected photon energy it is in principle possible to measure six angular distribution curves via different paths as in Fig(8). Unfortunately, no radiative decay rates are

Angular distributions: Er3+

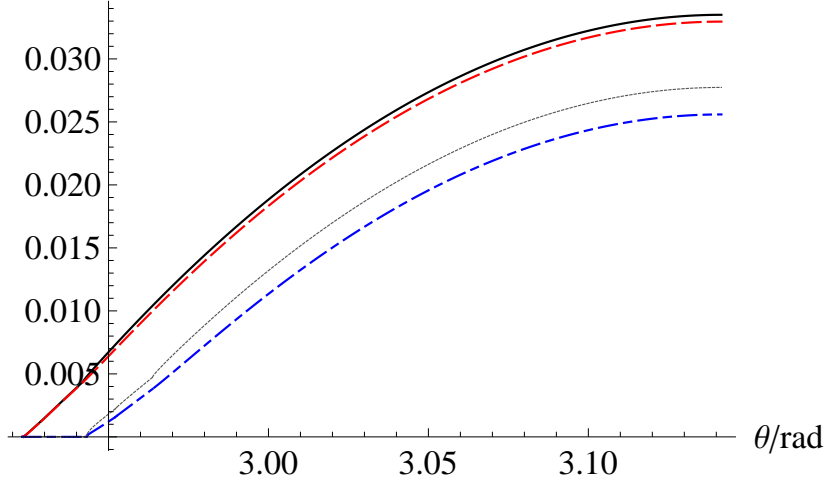


Figure 7: Raman trigger angular distribution given by $8\pi \sum_{ij} F_{ij}(\theta)$ in eV^2 unit, assuming different $r = 24.08$ in path B of $\text{Er}^{3+}:\text{Cs}_2\text{NaYF}_6$: Dirac NH cases of smallest mass 5 meV in solid black, 50 meV in dotted black, Majorana NH cases of smallest mass 5 meV in dashed red, and 50 meV in dash-dotted blue. CP violating phases are assumed to vanish.

not known for this crystal, and one cannot predict RANP rates precisely. Moreover, Er sites can be at either of two Y sites one of which has no inversion center, and one needs to calculate decay rates in this situation. It would however be interesting to pursue an experimental scheme using ceramic or poly-crystal of this target in a hollow of Bragg fiber.

Acknowledgements

We thank F. Chiossi at Padova for bringing the paper [8] to our attention and M. Tanaka at Osaka for discussions on the Bragg fiber. This research was partially supported by Grant-in-Aid 19K14741(HH), 19H00686(NS), 17H02896(AY) and 17H02895(MY) from the Ministry of Education, Culture, Sports, Science, and Technology.

References

- [1] H. Hara and M. Yoshimura, arXiv: 1904.03813v1 (2019) and Eur.Phys.J. **C79** 684(2019).
- [2] H. Hara, N. Sasao, and M. Yoshimura, arXiv: 1909.06554 (2019) to be revised.
- [3] A. Fukumi et al., Prog. Theor. Exp. Phys. (2012) 04D002.

Angular distributions: Er3+

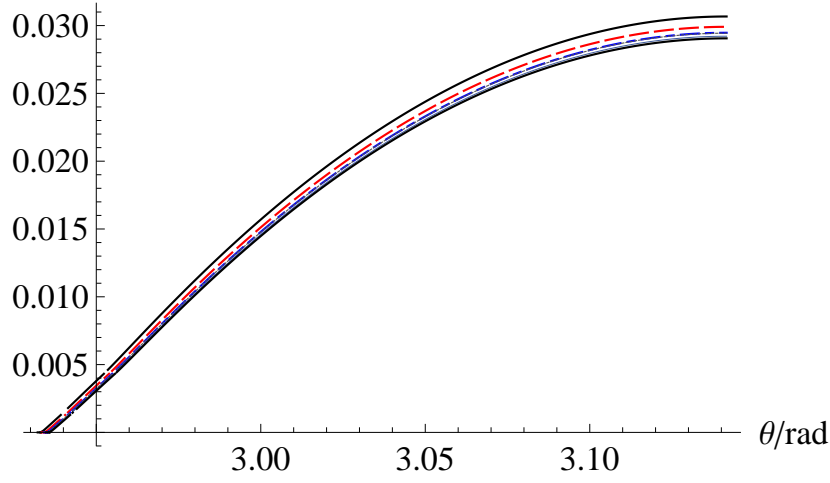


Figure 8: Angular distribution of RANP trigger photon given by $8\pi \sum_{ij} F_{ij}(\theta)$ in eV^2 unit using Stark levels within $^4I_{13/2}$ manifold in scheme II of $\text{Er}^{3+}:\text{Y}_2\text{O}_3$. Smallest neutrino mass of $m_1 = 10 \text{ meV}$'s of Majorana NH with $r = 24.08$. De-excitation path via 6510, 6542, 6588, 6594, 6684, 6840, 6867 cm^{-1} in increasing rate order.

- [4] Y. Miyamoto et al., PTEP, 113C01 (2014). Y. Miyamoto et al., PTEP, 081C01 (2015). T. Hiraki et al., arXiv:1806.04005 [physics.atom-ph], and J. Phys. B: At. Mol. Opt. Phys. **52** 045401 (2019).
- [5] M. Tanaka, K. Tsumura, N. Sasao, and M. Yoshimura, Prog. Theor. Exp. Phys. 2017, 043B03 (18 pages).
- [6] M. Tanaka, K. Tsumura, N. Sasao, S. Uetake, and M. Yoshimura, paper in preparation.
- [7] X. Zhou et al., J. Phys. Chem. C **111**, 683 (2007).
- [8] P.A. Loiko et al., J. Luminescence, **185**, 279 (2017).
- [9] J.B. Gruber et al., J. Applied Phys. **108**, 023109 (2010).
- [10] M. Yoshimura, N. Sasao, and M. Tanaka, Prog. Theor. Exp. Phys. **2015**, 053B06 (1015).
- [11] J.H. Van Vleck, J. Chem. Phys. **41**, 67 (1937).
- [12] B.R. Judd, Phys.Rev.**127**, 750(1962). G.S. Ofelt, J. Chem. Phys. **37**, 511 (1961).
- [13] For a review of neutrino oscillation experiments and neutrino properties derived from these data, see Particle Data Group Collaboration, M. Tanabashi et al., Phys. Rev. D 98 030001 (2018).
- [14] J. D. Joannopoulos, S. G. Johnson, J. N.Winn, and R. D. Meade, *Photonic Crystals*, (Princeton University Press, Princeton, 2008), 2nd ed.